Extended x-ray absorption fine structure studies of the atomic structure of nanoparticles in different metallic matrices

2009 J. Phys.: Condens. Matter 21 183002

(http://iopscience.iop.org/0953-8984/21/18/183002)

J. Phys.: Condens. Matter **21** (2009) 183002 (17pp) doi:10.1088/0953-8984/21/18/183002

TOPICAL REVIEW

Extended x-ray absorption fine structure studies of the atomic structure of nanoparticles in different metallic matrices

S H Baker[1], **M Roy, S J Gurman and C Binns**

Department of Physics and Astronomy, University of Leicester, Leicester LE1 7RH, UK

E-mail: bak@le.ac.uk

Received 13 October 2008, in final form 25 February 2009
Published 6 April 2009
Online at stacks.iop.org/JPhysCM/21/183002

Abstract

It has been appreciated for some time that the novel properties of particles in the size range 1–10 nm are potentially exploitable in a range of applications. In order to ultimately produce commercial devices containing nanosized particles, it is necessary to develop controllable means of incorporating them into macroscopic samples. One way of doing this is to embed the nanoparticles in a matrix of a different material, by co-deposition for example, to form a nanocomposite film. The atomic structure of the embedded particles can be strongly influenced by the matrix. Since some of the key properties of materials, including magnetism, strongly depend on atomic structure, the ability to determine atomic structure in embedded nanoparticles is very important. This review focuses on nanoparticles, in particular magnetic nanoparticles, embedded in different metal matrices. Extended x-ray absorption fine structure (EXAFS) provides an excellent means of probing atomic structure in nanocomposite materials, and an overview of this technique is given. Its application in probing catalytic metal clusters is described briefly, before giving an account of the use of EXAFS in determining atomic structure in magnetic nanocomposite films. In particular, we focus on cluster-assembled films comprised of Fe and Co nanosized particles embedded in various metal matrices, and show how the crystal structure of the particles can be changed by appropriate choice of the matrix material. The work discussed here demonstrates that combining the results of structural and magnetic measurements, as well as theoretical calculations, can play a significant part in tailoring the properties of new magnetic cluster-assembled materials.

Contents

[1] Author to whom any correspondence should be addressed.

1. Introduction

Particles with sizes in the range 1–10 nm lie at the boundary between single atoms and bulk materials. For some time, it has been appreciated that the novel chemical, electronic and magnetic behaviour displayed by nanoparticles can potentially be exploited in a range of applications, including catalysis and the development of new magnetic materials. In order to realize this potential and produce commercial devices that incorporate nanosized particles, an important first step is to develop the ability to prepare macroscopic samples, which contain the nanoparticles of interest embedded in a matrix of a different material. A range of techniques have been used to prepare such cluster-assembled materials, but the most flexible is a co-deposition technique involving the use of a cluster source, as used by various groups [1–3]. As described in more detail in section 2, this technique produces films in which there is a high degree of control over the nanostructure.

It is clearly important to check that the novel, potentially exploitable, properties of interest in nanoclusters are maintained (or at least not too adversely affected) by embedding them in a matrix of another material. For example, as described at the start of section 5, size-related enhancements are expected in the atomic magnetic moments of nanoclusters of magnetic materials [4]. Enhanced magnetic moments measured for supported size-selected Fe clusters [5–7] were found to be maintained and indeed enhanced when coated in Co [6, 8]. It is also important to determine what effect the matrix has on the atomic structure within the clusters. For many years, ultra-thin metal films with atomic structures different from that of the corresponding bulk material have been grown by epitaxial growth on a suitable single crystal substrate e.g. Fe films on Cu [9–14]. It is therefore likely that the atomic structure in nanoclusters will be strongly affected and possibly changed to a different crystalline type by embedding the clusters in a suitable matrix. Since the relationship between structure and physical properties is one of the most fundamental in materials, it is clearly essential for the development of new nanocomposite materials to be able to determine the atomic structure in embedded nanoclusters.

Experimental techniques that can be applied to structure determination include direct imaging methods such as high resolution transmission electron microscopy (HRTEM), and x-ray techniques such as x-ray diffraction (XRD) and small angle x-ray scattering (SAXS). The element-specific and local nature of extended x-ray absorption fine structure (EXAFS), however, makes it an ideal probe of atomic structure in nanocomposite materials.

This review focuses on magnetic nanoclusters embedded in metallic matrices. Initially, some of the ways of producing cluster-assembled materials are briefly described in section 2. Section 3 summarizes the key points relating to EXAFS, without attempting to provide a review of the technique itself for which the reader is directed elsewhere [15–19]. By way of introduction to the published work, section 4 describes the application of EXAFS to various types of catalytic cluster, although usually in hosts such as alumina or silica rather than a metallic matrix. In section 5, the use of EXAFS to probe the atomic structure of embedded magnetic clusters is described. We show that combining the results of EXAFS and magnetic measurements, as well as theoretical calculations, not only helps to develop a better understanding of the system under study but should enable the tailoring of properties in new nanocomposite magnetic materials.

2. Preparation of cluster-assembled films

There are a variety of methods for preparing materials with a granular microstructure which do not rely on the use of a dedicated cluster source. One of the more widely used techniques is co-sputtering where cluster formation is reliant on immiscibility between cluster and matrix material. For example, granular films consisting of Fe clusters in a Cu, Ag or Au matrix [20], and Co clusters embedded in Cu [21], have been deposited in this way. As well as magnetic granular films, co-sputtering can also be used to deposit ultra-hard coatings such as nc-TiN/a-SiN-nanocrystallites of TiN embedded in amorphous silicon nitride [22]. Control over sample nanostructure is, however, semi-empirical and is achieved by varying deposition parameters such as substrate temperature, power supplied to the plasma, etc. Magnetic granular alloys, for example CuCo alloys, have also been prepared by melt-spinning [23, 24], with subsequent annealing required to encourage precipitation of Co granules. In addition, ball milling has been tried as a means of synthesizing two-phase mixtures of immiscible metal systems, for example dispersions of nanometre-sized Pb particles in an Al matrix from elemental powders of Al and Pb [25]. However, as for the co-sputtering process, control over sample nanostructure is at best semi-empirical. Aside from the techniques referred to above, wet chemistry methods are extensively used to make metal clusters of interest to catalysis such as silica-supported Pd–Au clusters [26, 27] and zeolite-supported Rh–Pt clusters [28].

If available, however, direct cluster deposition offers appreciably more control in the preparation of cluster-assembled films than do other techniques. Over the past 20 years, a variety of cluster deposition sources have been developed and the reader is referred to existing reviews [29–31] for more detailed information. Figure 1 illustrates schematically the deposition of a granular film on a substrate by co-deposition from a cluster source and a molecular beam epitaxy (MBE) source. The cluster source provides a beam of size-selected clusters while the MBE source provides the matrix material. By adjusting the deposition rates of clusters and matrix material at the sample (measurable by e.g. a quartz crystal thickness monitor), the filling fraction of clusters in the film can be controlled accurately and independently of the cluster size. Hence, with the ability to size-select the clusters, the co-deposition technique affords direct control over the sample nanostructure. An additional advantage of this technique is the ability to deposit granular mixtures of miscible materials, for example granular Fe–Co by depositing Fe nanoclusters in a Co matrix or vice versa [3, 32].

A number of groups have developed and now routinely use the technique described above to produce films of cluster-assembled materials [1–3, 33]. For example, the Lyon group

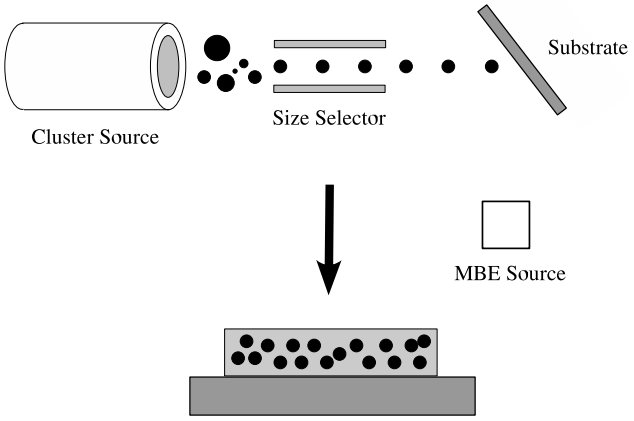

Figure 1. Schematic diagram illustrating co-deposition of nanoparticles from a cluster source and matrix material from an MBE source to form a cluster-assembled film.

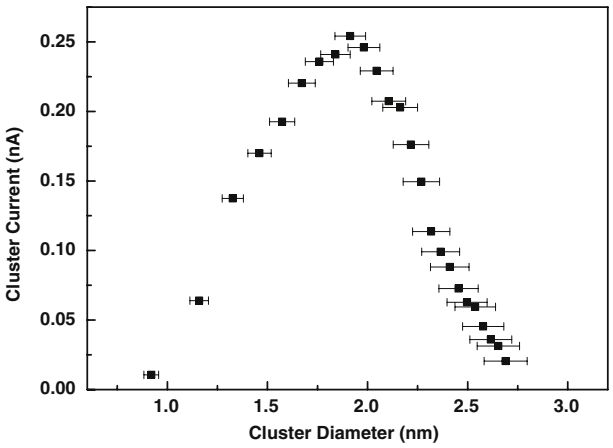

Figure 2. Distribution of sizes (diameters) for Co clusters typically produced in the Leicester group's gas aggregation cluster source.

uses a laser evaporation–gas aggregation source coupled to a UHV chamber containing various Knudsen cell sources [1], while the group at Rostock has a recently-developed continuous-arc cluster-ion-source (ACIS) [2]. In our own group, cluster-assembled films are deposited using a UHV-compatible thermal evaporation–gas aggregation source [34]; the source incorporates an axially mounted quadrupole mass filter, which allows either size-selection of the clusters or, more usually, *in situ* monitoring of these and the size distribution of the deposited clusters if size-selection is not required. Figure 2 shows the distribution of sizes typically produced in the source, in this case for Co clusters. Capping layers of Ag can be deposited in order to protect the cluster samples against oxidation after removal from the vacuum chamber.

3. EXAFS

3.1. Qualitative description of EXAFS process

Figure 3 illustrates the EXAFS process schematically. An x-ray photon with energy just greater than the threshold required

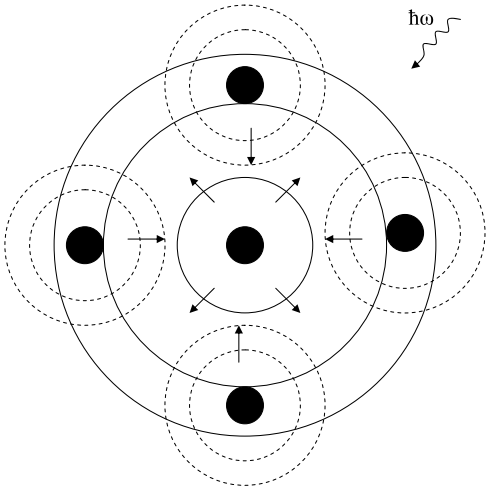

Figure 3. Schematic illustration of the EXAFS process. The atom at the centre absorbs an x-ray photon of energy $\hbar\omega$. A core level electron is emitted as a photoelectron wave, represented by the solid circles concentric with the central atom. The outgoing wave back-scatters off surrounding atoms. Interference effects occur between the outgoing and reflected waves. (Illustration is adapted from [35].)

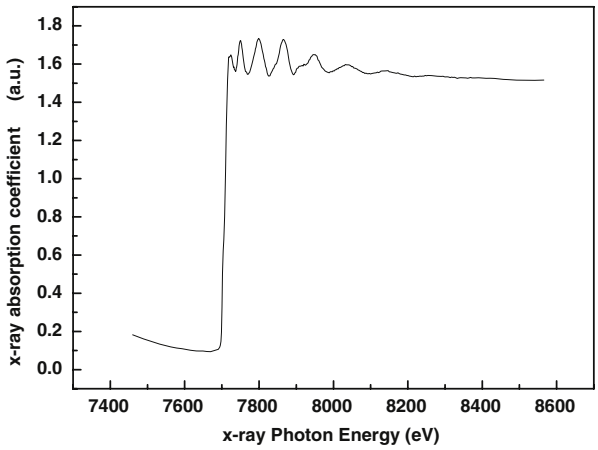

Figure 4. Co K edge absorption spectrum for a 150 Å film comprised purely of Co clusters.

to eject a core level electron is incident on the material of interest. Following absorption of the photon by a constituent atom in the material, a photoelectron is emitted. If the absorbing atom is surrounded by other atoms, as in a solid, the outgoing photoelectron wave will be back-scattered, leading to interference effects between back-scattered and outgoing waves. This in turn modulates the matrix elements for the absorption process. As the incident x-ray photon energy is increased beyond the threshold, the energy of the photoelectron increases; the corresponding electron wavelength decreases, and therefore constructive or destructive interference occurs depending on whether the interatomic distance is an integral or half-integral number of wavelengths respectively. Hence, for a solid, one observes 'fine structure' or oscillations in the x-ray absorption above an absorption edge. This is illustrated for the case of a 150 Å film of pure Co clusters [36] in figure 4, which clearly shows the fine structure above the Co K edge.

The amplitude of the oscillations in EXAFS depends on the number and electron scattering strength of the scattering atoms. Therefore, analysis of the EXAFS yields distances, number and identity of the near neighbours of the excited atom. Since the EXAFS is measured at an absorption edge for a known atom type, it is chemically specific. Also, EXAFS depends only on the local atomic environment due to the fact that only elastically scattered electrons can contribute to the interference and the elastic mean free path of electrons is short. The element-specific and local nature of EXAFS makes it an ideal probe of atomic structure in nanocomposite materials.

3.2. Semi-classical/quantum description of EXAFS

The absorption process can be treated semi-classically, describing the x-ray photon in terms of a classical electromagnetic field but using a quantum mechanical description for the electron. Within the dipole approximation, where the photon wavelength is large compared with the spatial extent of the excited core state, the absorption process can be treated using first order perturbation theory. Fermi's golden rule then gives for the transition probability (per unit time)

$$P = \frac{2\pi^2 e^2}{mc^2\omega}|\langle f|\mathbf{e}\cdot\mathbf{r}|i\rangle|^2\rho(E), \tag{1}$$

where $|i\rangle$ and $|f\rangle$ are the wavefunctions of the initial and final states of the electron respectively, $\rho(E)$ is the density of states at final energy E and $\mathbf{e}$ is the polarization vector of the electric field in the x-ray beam. ω is the angular x-ray frequency, and e and m the electron charge and mass respectively. $\rho(E)$ is well described by a free electron density of states and, hence, varies with the square root of energy. Therefore, the only factor that can give rise to the fine structure is the matrix element. Since the initial state wavefunction is fixed and does not vary with photon energy, it is the energy variation of the final state $|f\rangle$ (made up of the outgoing and back-scattered waves) that modulates the matrix element and, hence, gives rise to the fine structure in the x-ray absorption μ (governed of course by P).

The EXAFS signal $\chi(E)$ can be explicitly included in the x-ray absorption by writing the absorption coefficient μ as

$$\mu(E) = \mu_0(E)[1 + \chi(E)], \tag{2}$$

where μ_0 is the background absorption, physically corresponding to the absorption coefficient for an isolated atom. The photoelectron energy E (final state energy) is related to the final state wavevector k by

$$E = E_0 + \frac{\hbar^2 k^2}{2m}, \tag{3}$$

where E_0 is the energy of a free electron with zero momentum. Normally referred to as the threshold energy, E_0 cannot be placed precisely. However, when fitting experimental EXAFS data, it can be left as an adjustable parameter. Hence (in terms of k) the EXAFS is defined by

$$\chi(k) = \frac{[\mu(k) - \mu_0(k)]}{\mu_0(k)}. \tag{4}$$

3.3. Structural information in EXAFS

Initial theories proposed to describe the EXAFS function $\chi(k)$ were based on the plane wave approximation [37], which treats the electron waves as planar rather than spherical. For energies high enough above the edge ($\gtrsim$80 eV) this is valid. Although this restriction is a major limitation, the expression developed for $\chi(k)$ using the plane wave approximation illustrates very well the various structural parameters that affect the EXAFS, and is given below.

$$\chi(k) = -\sum_i s_0^2 \frac{N_i}{kr_i^2}|f_i(k,\pi)|\sin(2kr_i + 2\delta_i + \varphi_i)\mathrm{e}^{-2\sigma_i^2 k^2}\mathrm{e}^{-\frac{2r_i}{\lambda}}. \tag{5}$$

The sum is over atom types i. N_i is the number (coordination number) of atoms of type i at a distance r_i from the absorbing atom; each of these has a back-scattering amplitude $|f_i(k,\pi)|$. The first exponential factor in equation (5), the Debye–Waller factor, describes the effects of thermal and (in the case of an amorphous solid) structural or static disorder; σ_i^2 is the mean square variation in interatomic distances. The second exponential term in the expression for χ represents losses due to inelastic scattering, λ being the elastic mean free path of the photoelectron. A constant amplitude reduction factor s_0^2 approximates losses due to multiple electron excitations at the absorbing atom. Finally, δ_i is the phase shift experienced by the photoelectron through the central (absorbing) atom potential, while φ_i is the phase of the back-scattering factor.

However, for energies in the range (10–80 eV) above the absorption edge, the spherical nature of the electron waves can no longer be neglected and the full curved wave theory introduced by Lee and Pendry [38] must be used. This was simplified by Gurman *et al* [39] for cases where the angle between the polarization and displacement vectors (equation (1)) is randomly distributed, for example in amorphous materials and many nanocrystalline samples, into the fast curved wave theory.

3.4. Measurement of EXAFS data

Development of intense dedicated synchrotron radiation sources, from second generation sources such as the one at Daresbury Laboratory to third generation sources such as the Diamond Light Source, has enabled EXAFS experiments to be carried out over viable timescales. The conventional method of measuring EXAFS uses transmission geometry, where the incident x-ray intensity I_0 and intensity I transmitted through a thin foil of thickness d are measured as a function of photon energy. Ionization chambers containing rare gas mixtures are normally used to measure I and I_0. The absorption coefficient μ is then obtained straightforwardly from

$$I = I_0\mathrm{e}^{-\mu d}. \tag{6}$$

Double-crystals or channel-cut crystals, often Si, are used to monochromatize the x-ray beam on most EXAFS beamlines. It is common practice to detune the monochromator slightly in order to reduce higher harmonic content; in our own work, harmonic rejection is typically set at ~70% [32].

In the case of very thin or dilute samples, the EXAFS signal is swamped by the large background absorption in transmission measurements, and a more sensitive detection method such as fluorescence is needed. This is an indirect technique, in which the core hole created by the absorption event decays radiatively giving rise to x-ray fluorescence at a characteristic photon energy. For example, at a K edge the 1s core hole left by the photoelectron is filled by a p electron from the L shell. Hence, by tuning to the fluorescent x-ray energy, only the excited atoms in the sample are monitored, leading to appreciable increases in sensitivity. The spectrum in figure 3 for the Co cluster film was recorded using fluorescence detection. A multi-element solid state detector is normally used to detect the fluorescent x-rays. Typically, this is mounted perpendicular to the incident x-ray beam, in order to minimize the effects of scattered x-rays, with the sample at 45° to both. It is important to minimize self-absorption of fluorescent photons; for very thin samples, whose thickness is much less than an absorption length, or dilute samples where only a small part of the total absorption is due to the edge being measured, self-absorption can be safely neglected.

3.5. Fitting experimental EXAFS data

The first step in reducing the measured x-ray absorption spectrum to obtain the EXAFS $\chi(k)$ is to subtract off the background absorption $\mu_0(k)$. This can conveniently be done by fitting a smooth function, such as a low order polynomial (or combination of low order polynomials), to the measured absorption both below and above the absorption edge. The position of the edge E_{edge} is normally taken to lie at the point at which the first derivative with respect to energy is a maximum. The photoelectron energy E is then related to photon energy (selected by the monochromator) by

$$E = h\omega - E_{\text{edge}} \tag{7}$$

and to wavevector k by equation (3). Finally, the spectrum is normalized as described by equation (4) to give the EXAFS spectrum $\chi(k)$. In some cases [40], authors have normalized to the height of the edge step $\Delta\mu_0(k)$. Figure 5 shows $\chi(k)$ (weighted by k^3 for the reason discussed below) for the Co cluster film whose Co K edge absorption spectrum is shown in figure 4.

Following background-subtraction and normalization, the experimental $\chi(k)$ can then be analysed by calculating $\chi(k)$ and optimizing the least squares fit to the measured spectrum by adjusting the structural parameters. Structural parameters varied in the fitting procedure are those that appear in equation (5) i.e. N_i, r_i and σ_i^2, as well as the identity of the scattering atoms which determines $|f_i(\pi)|$. In general, it is possible to achieve an accuracy of ± 0.02 Å for the fitted values of r_i, and $\pm 10\%$ for N_i. There are a variety of packages for analysing and fitting EXAFS data referred to in the literature e.g. EXCURV [41], UWXAFS [42] IFEFFIT [43] and others[2]. In our recent work e.g. [32], we have analysed EXAFS data with the EXCURV98 program [41]

[2] A comprehensive list of EXAFS data analysis packages is available on the website of the International XAFS Society, http://ixs.iit.edu.

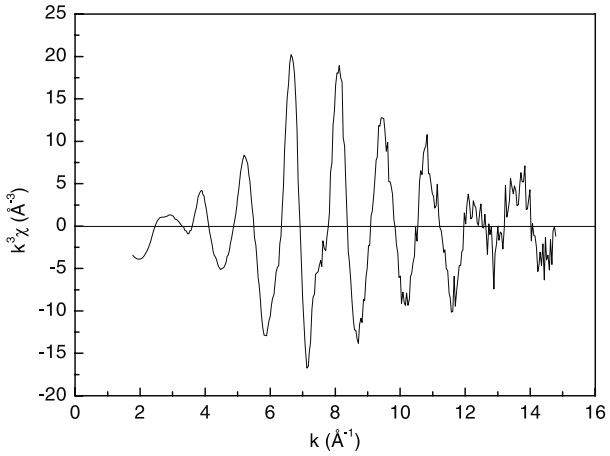

Figure 5. EXAFS spectrum χ, weighted by k^3, for the 150 Å Co cluster film whose Co K edge absorption spectrum is shown in figure 4.

which uses fast curved wave theory [39] to calculate χ. Most data analysis packages allow the calculation of $|f_i(k,\pi)|$ and the scattering phase shifts using a complex exchange and correlation potential, for example the Hedin–Lundqvist potential as used in EXCURV98. This models inelastic processes and thus includes some, if not all, of the reduction effects in the amplitude of the EXAFS [44]; in the simple plane wave expression for $\chi(k)$, these effects are represented by the factors $e^{-2r/\lambda}$ and s_0^2.

Data analysis can be performed either in k-space by fitting directly to the EXAFS or in real space where the fit is to the Fourier transform of the EXAFS function. The spectrum is normally weighted by k^n, most commonly with $n = 3$, in order to counteract the effects of the decrease in $|f_i(\pi)|$, which occurs with increasing energy and of the Debye–Waller factor; a function with constant amplitude yields a sharper Fourier transform. In general, k-space analysis is more reliable as it avoids problems associated with a finite range Fourier transform. Figure 6 shows $k^3\chi$ and its Fourier transform for the Co cluster film referred to earlier (see figures 4 and 5). The data was fitted using EXCURV98 which fits to the EXAFS, and not to the Fourier transform. In the figure, the experimental data is indicated by the full lines, while the dashed lines represent the fit to $k^3\chi$ and Fourier transform of the fit. In this case, the fit is consistent with the hcp crystal structure of bulk Co (see table 1). It should be noted that the Fourier transform in the figure (and also the Fourier transforms in figures presented later in this article) are phase-corrected, the correction being calculated from the first-shell back-scattering factor. The Fourier transform is useful as a preliminary analysis, giving a good idea of the amount of experimental information in the experimental EXAFS spectrum, and (with phase correction) fixing the interatomic distances reasonably well. (Multiplying by r^2 would then essentially yield the radial distribution function, at least for a monatomic material. In the case of a multi-atom compound, the phase correction only correctly affects the atoms for which the phase was calculated; hence, strictly speaking, the radial distribution function cannot

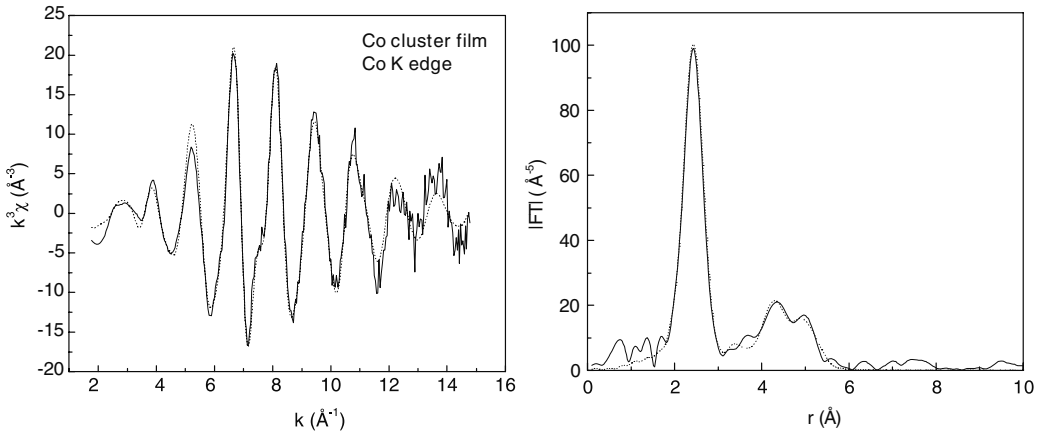

Figure 6. $k^3\chi$ and Fourier transform of $k^3\chi$ for the 150 Å Co cluster film for which absorption data is displayed in figure 4. The full lines represent the data and Fourier transform of the data while the dashed lines represent the fit to the data and Fourier transform of the fit.

be determined although all peaks appear close to their true positions.)

Many of the EXAFS analysis programs referred to above allow the possibility to take multiple scattering effects into account; in our own work (using EXCURV98) we have done so for in-line structures, where multiple scattering is most important. Specifically: (i) when fitting to a bcc structure, we have allowed for multiple scattering between shells 1 and 5 (at least in cases where including a fifth shell in the fit to the data is statistically significant) (ii) when fitting to an hcp structure, we have allowed for multiple scattering between shells 1 and 6 (where fitting a sixth shell is statistically significant) (iii) when fitting to an fcc structure we have allowed for multiple scattering between shells 1 and 4.

3.6. Comments relating to EXAFS analysis for clusters

For small enough clusters (diameter ∼1 nm), one should expect to detect decreases in the coordinations N_i compared with those for the same crystal structure in the corresponding bulk material. These effects have been seen in Au_{55} clusters, for example, where first-shell coordinations N_1 of between 5 and 8 [45, 46] have been measured; this compares with the figure of 12 for the fcc structure, adopted by bulk Au. Furthermore for a given crystal structure, the shape of the cluster will affect the coordinations. For example, an fcc cluster can be icosahedral, cuboctahedral etc; the decrease in coordination numbers with decreasing cluster size will be different depending on the shape of the fcc cluster, as described by Frenkel *et al* [47] for supported Pt clusters. However, the differences are usually small and, given the experimental errors in measured coordinations, it is generally difficult to determine cluster shape from EXAFS data alone.

Other structural effects associated with clusters, detected in EXAFS, include a non-zero value for the static contribution σ_s^2 to the total disorder σ^2 [47]. This can be isolated from the dynamic (temperature-dependent) contribution by measuring at different temperatures. For supported Pt clusters [47], σ_s^2 was found to increase markedly with decreasing cluster size; it was suggested that the most plausible explanation for the static disorder was a relaxation in bond lengths for atoms at the cluster surface.

In our own work on magnetic nanocomposite films, where the mean cluster size is ∼2 nm (see figure 2) or ∼260 atoms per cluster, the fitted values of N_i sometimes hint at size-related reductions [32, 48] although the experimental errors involved generally include the bulk value. In any case, our main interest has generally been to detect any change in crystal structure in the (wholly embedded) clusters. Therefore, when fitting to a particular crystal structure, we normally hold the coordinations N_i fixed at the values associated with that structure for the bulk but allow σ_i^2 and r_i to vary freely. Table 1 gives the fit parameters obtained in such a constrained fit to the EXAFS data in figure 6 for the Co cluster film, along with the known interatomic distances in bulk hcp Co. The fit is consistent with the hcp structure, with agreement between the fit values and bulk Co values for r_i best for the inner shells. As we have also seen for Fe clusters embedded in Ag [48] and Co clusters in Fe [32], the constrained fitting procedure does not affect the fit values obtained for r_i.

As described in section 3.3, disorder (variation in interatomic distances) can be taken into account in expressions for EXAFS $\chi(k)$ by means of Debye–Waller factors. This effectively assumes a Gaussian pair distribution, and ignores any anharmonicity in the pair interaction potential. Anharmonic effects can be taken into account by means of the third cumulant $\sigma_i^{(3)}$ of the pair distribution [49–51] which can be included in the expression for $\chi(k)$ (see equation (5)), as below.

$$\chi(k) = -\sum_i s_0^2 \frac{N_i}{kr_i^2} |f_i(k,\pi)| \times \sin(2kr_i - \tfrac{4}{3}\sigma_i^{(3)}k^3 + 2\delta_i + \varphi_i) e^{-2\sigma_i^2 k^2} e^{-\frac{2r_i}{\lambda}}. \quad (8)$$

In systems such as small clusters, where non-Gaussian pair distribution functions are possible, it is important in principle to consider anharmonic effects when analysing EXAFS data; ignoring these could lead to an unphysically shortened value in the fit value for the interatomic distance [52]. Such analysis, for example, is well described for supported Pt [47] and Au [51] particles, although in the case of the Au particles the

Table 1. Structural parameters r_j, $2\sigma_j^2$ (interatomic distance, Debye–Waller factor respectively) obtained from fits to the EXAFS for a Co cluster film, a 4.1% VFF Co/Ag film and a Co MBE film. Also included are the interatomic distances and coordinations N_j for hcp Co. The coordinations were held fixed at hcp values during the fits.

	Shell 1	Shell 2	Shell 3	Shell 4	Shell 5	Shell 6
HCP Co	$r_1 = 2.50$ Å[a]	$r_2 = 3.54$ Å	$r_3 = 4.07$ Å	$r_4 = 4.34$ Å	$r_5 = 4.78$ Å	$r_6 = 5.01$ Å
	$N_1 = 12$[a]	$N_2 = 6$	$N_3 = 2$	$N_4 = 18$	$N_5 = 12$	$N_6 = 6$
Co cluster film	$r_1 = 2.49 \pm 0.01$ Å	$r_2 = 3.51 \pm 0.03$ Å	$r_3 = 3.98 \pm 0.04$ Å	$r_4 = 4.36 \pm 0.02$ Å	$r_5 = 4.84 \pm 0.02$ Å	
	$2\sigma_1^2 = 0.016 \pm 0.001$ Å^2	$2\sigma_2^2 = 0.034 \pm 0.007$ Å^2	$2\sigma_3^2 = 0.017 \pm 0.009$ Å^2	$2\sigma_4^2 = 0.025 \pm 0.003$ Å^2	$2\sigma_5^2 = 0.023 \pm 0.004$ Å^2	
4.1% VFF Co/Ag	$r_1 = 2.49 \pm 0.01$ Å	$r_2 = 3.44 \pm 0.06$ Å	$r_3 = 4.00 \pm 0.04$ Å	$r_4 = 4.34 \pm 0.03$ Å	$r_5 = 4.84 \pm 0.04$ Å	
	$2\sigma_1^2 = 0.021 \pm 0.001$ Å^2	$2\sigma_2^2 = 0.052 \pm 0.021$ Å^2	$2\sigma_3^2 = 0.011 \pm 0.008$ Å^2	$2\sigma_4^2 = 0.043 \pm 0.009$ Å^2	$2\sigma_5^2 = 0.030 \pm 0.010$ Å^2	
MBE Co film	$r_1 = 2.50 \pm 0.01$ Å	$r_2 = 3.52 \pm 0.02$ Å	$r_3 = 4.03 \pm 0.04$ Å	$r_4 = 4.36 \pm 0.01$ Å	$r_5 = 4.85 \pm 0.01$ Å	$r_6 = 5.19 \pm 0.03$ Å
	$2\sigma_1^2 = 0.013 \pm 0.001$ Å^2	$2\sigma_2^2 = 0.022 \pm 0.003$ Å^2	$2\sigma_3^2 = 0.015 \pm 0.007$ Å^2	$2\sigma_4^2 = 0.019 \pm 0.002$ Å^2	$2\sigma_5^2 = 0.014 \pm 0.002$ Å^2	$2\sigma_6^2 = 0.027 \pm 0.007$ Å^2

[a] The first shell in hcp Co is actually split, with 6 atoms at 2.497 Å and 6 atoms at 2.507 Å. The experimental errors do not allow us to resolve these.

fitted nearest neighbour distance was the same whether or not the third cumulant was used in the analysis. In our own work on embedded metal clusters, we have generally found that including a third cumulant into the EXAFS analysis does not alter the interatomic distance or improve the fit significantly. For example, for the pure Co cluster film whose EXAFS data is presented in figure 6, analysis with $\sigma_1^{(3)} = 0$ (fixed) yields $r_1 = 2.50 \pm 0.01$ Å (see table 1). Including a third cumulant in the analysis yields $\sigma_1^{(3)} = (1.8 \pm 2.0) \times 10^{-4}$ Å^3, without any significant improvement in fit or change in r_1.

4. Catalytic metal clusters

The enhancement in chemical reactivity of small metal clusters (relative to the bulk material) is of course well known, and this has led to their widespread use in heterogeneous catalysts. Typically, heterogeneous catalysts consist of metallic nanosized clusters (diameter ∼1 nm) supported on an oxide carrier such as silica or alumina. Much of the published work describing the use of EXAFS to investigate atomic structure in nanosized clusters refers to catalytic clusters. Clearly, a better knowledge of atomic and electronic structure in metal clusters will be valuable in furthering our understanding of how catalysis is facilitated i.e. which active sites are involved in physi/chemisorption.

Ligand-stabilized metal clusters can be considered as model compounds for the catalytic properties of small metal clusters. A number of authors [45, 46, 53] have published good quality L_3 edge EXAFS for Au_{55} and Au_{11} clusters stabilized by a variety of organic ligands. These studies showed that the fcc structure of bulk Au was retained in the clusters, but with a contraction in the nearest neighbour distance of 0.05–0.1 Å for Au_{55} and up to 0.2 Å for Au_{11}. This effect has also been observed in larger Au clusters prepared by wet chemical techniques, with diameters between 3 and 7 nm [54], as well as in vacuum deposited Au clusters, with diameters in the range 1–6 nm [51, 55]. Contractions of 0.1 Å in nearest neighbour distance have also been found in silica-supported (fcc) Pt clusters, at least for bare clusters [56]; coverage of the clusters by chemisorbed hydrogen, however, causes the nearest neighbour distance to revert to the bulk Pt value. Not all catalytic metal clusters show such contractions. For example, EXAFS experiments on CeO_2 supported Ag clusters [57] and also Cu clusters on alumina [58], indicate that first and second nearest neighbour distances are essentially the same as in bulk Ag and Cu, respectively.

In a variety of applications, including chemical manufacturing and control of vehicle pollution, supported bimetallic catalysts are used. The reactivity and selectivity of metal clusters can be dramatically affected by the presence of a second metal component [59–64]. For example, in the reaction of dihydrogen and dioxygen to form water over supported Pd and PdAu catalysts, the turnover rate per surface Pd atom when a PdAu catalyst is used is 50 times greater than when using a pure Pd catalyst [61]. A knowledge of the structure of bimetallic clusters will involve not only the crystal structure, cluster size and shape but also the distribution of the two metals within the cluster. In the case of silica-supported PdAu clusters, EXAFS measurements indicate that the distribution of constituent atoms within the clusters depends on cluster composition [65, 66]. In slightly Pd-rich clusters (∼$Pd_{0.6}Au_{0.4}$) Pd atoms 'decorate' a Au-rich core [65, 66], whereas for equiatomic compositions ($Pd_{0.5}Au_{0.5}$) homogeneous alloy clusters are formed [66]. Other bimetallic catalytic clusters for which EXAFS has been used to probe atomic structure include RhPt clusters on a zeolite support [67]; the authors were unable to draw any conclusions from the data regarding compositional homogeneity in the particles, although the results did indicate the lack of substantial surface enrichment.

In two-element systems it is useful (if possible) to measure the EXAFS at both constituent edges, as was done in the studies on PdAu clusters referred to above [66], where both Pd K and Au L_3 edge spectra were recorded. This allows one to check for consistency between results obtained from analysis of the EXAFS for the two constituent edges. Clearly, the heterogeneous interatomic distance determined from both edges should be the same i.e. for the PdAu clusters

$$r_{\mathrm{Pd-Au}} = r_{\mathrm{Au-Pd}}. \tag{9}$$

Also the heteronuclear coordination numbers should satisfy the conservation equation, which for the PdAu clusters is

$$x_{\mathrm{Pd}} N_{\mathrm{Pd-Au}} = x_{\mathrm{Au}} N_{\mathrm{Au-Pd}} \tag{10}$$

where $N_{\mathrm{Pd-Au}}$ is the heteronuclear coordination determined from the Pd edge EXAFS, $N_{\mathrm{Au-Pd}}$ is the heteronuclear coordination determined from the Au edge EXAFS, and x_{Pd} and x_{Au} are the atomic fractions of Pd and Au respectively. In other words, the number of Pd–Au bonds is the same whether viewed from a Pd or a Au atom. Adopting consistency criteria helps to ensure that physically meaningful results are obtained from the data analysis.

5. Magnetic cluster-assembled films

A number of groups [23, 32, 68] have used EXAFS to probe the atomic structure in magnetic transition metal clusters when embedded in a matrix of a different metal. However, there have generally been fewer EXAFS studies of nanoscale clusters in a metallic environment than in hosts such as silica or alumina (as for catalytic clusters, for example). Arguably, the simplest metallic nanostructure involving clusters, and for which EXAFS experiments have been carried out, are single element nanocrystalline metal samples [69, 70].

Early EXAFS experiments on nanocrystalline metals were carried out by workers in the Engineering community [70–73], interested in probing the link between mechanical properties and structure in nanophase metals; in particular they were interested in establishing the nature of the grain boundary structure. For a typical polycrystalline metal, where the grain size is a few microns and the grain boundary fraction is ∼0.01%, it is well known that shrinking the grain size leads to increases in hardness due to a hindering of the dislocation motion by an increase in grain boundary fraction. If the grain size is reduced to a few nm, the grain boundary fraction approaches ∼50%. For nanocrystalline samples of various metals, increases in hardness by factors of between

2 and 7 have been recorded relative to their coarser grained counterparts [74]. Obtaining a detailed picture of the structure in the grain boundaries is important in understanding the mechanical properties of new nanostructured materials. EXAFS experiments on nanocrystalline Cu [71], where the grain size was in the range 10–24 nm, appeared to suggest that the grain boundaries were gas-like, lacking even short range order. However later measurements, also on Cu [70], where the grain sizes studied were 13 and 24 nm, indicated that the short range order of polycrystalline samples was retained in the grain boundaries. As newer multi-component nanocomposite hard coatings continue to be developed, it seems clear that EXAFS can play an important role in probing the structure of these new materials thanks to its non-invasive, element-specific nature. It is fair to say, though, that much of the work describing the use of EXAFS to investigate atomic structure in metallic cluster-assembled materials relates to magnetic materials, and it is these on which we now focus.

Enhanced magnetic moments in nanosized clusters of magnetic materials are expected due, in part, to an enhanced proportion of under-coordinated atoms at the surface of the cluster. This gives rise to a narrowing of the valence band which leads to an increase in the density of states at the Fermi level and, hence, an increase in the atomic spin moment [4]. An increase in the orbital spin moment is also expected due to less effective quenching by a reduced symmetry crystalline field. Further contributions to novel behaviour in magnetic nanoclusters come from the quantum size effect [75, 76] and modified electron screening behaviour. Confirmation of enhanced magnetic moments in free cluster beams of Fe, Co and Ni [4, 77] was provided by Stern–Gerlach experiments. Subsequently, x-ray magnetic circular dichroism (XMCD) experiments confirmed that for transition metal clusters such as Fe [5–7] supported on a substrate, both spin and orbital moments were enhanced.

In addition to the size-related effects outlined above, the crystal structure adopted by clusters will play an important role in determining their magnetic properties. Total energy calculations have been performed by various authors [78–83] for bulk transition metals; different atomic magnetic moments are predicted for different crystal structures (for a given metal). It is now well established that metastable atomic structures, different from that of the corresponding bulk metal, can be seen in ultra-thin metal films grown epitaxially on a substrate of a different metal. For example, although Fe adopts a bcc structure in bulk form at room temperature, it is possible to grow fcc Fe films a few monolayers thick on a Cu substrate [9–14]. Similarly, the atomic structure of magnetic nanosized clusters is likely to be strongly affected by embedding them in the matrix of a different metal. The possibility of 'engineering' the atomic structure to produce a given set of magnetic properties would clearly be valuable in the drive to develop new high performance magnetic materials assembled from clusters.

5.1. Co clusters

Total energy calculations carried out by a number of authors show that for bulk Co the hcp and fcc phases are energetically very close to one another [80, 83]. This implies that, although hcp is the structure adopted by bulk Co at room temperature, it should be possible to stabilize the fcc structure in Co without too much difficulty. Indeed, fcc Co films up to 1000 Å thick have been grown epitaxially on Cu(110) [84]. It therefore seems reasonable to expect that the fcc structure might also be stabilized in Co clusters by embedding them in an appropriate metal matrix.

The discovery that metastable granular Co–Cu alloys exhibit giant magnetoresistance (GMR) [85, 86] stimulated a great deal of research activity in this and similar alloy systems. Although Co and Cu are immiscible at room temperature, the techniques used to prepare the alloy material, such as melt-spinning or sputtering, give rise to a solid solution of Co in Cu. Subsequent thermal annealing causes the precipitation of small Co clusters. The observation of GMR is then a result of spin-dependent scattering of conduction electrons due to the presence of small magnetic Co clusters embedded in a non-magnetic Cu (or Cu-rich CuCo alloy) matrix. A number of authors have used EXAFS to probe the atomic structure in the Co precipitates [23, 24, 87, 88]. In all these studies, the samples were prepared by melt-spinning and subsequent annealing, and the matrix was a Cu-rich CuCo alloy e.g. $Cu_{85}Co_{15}$ [23], $Cu_{90}Co_{10}$ [24]. Prior to annealing, Co K edge EXAFS performed on these samples was consistent with an fcc structure, as would be expected for Cu or (as here) a Cu-rich alloy. Progressive annealing caused a gradual decrease in the average Co nearest neighbour distance from the Cu–Cu distance (∼2.55 Å) towards the value found in metallic Co (∼2.50 Å whether fcc or hcp), consistent with the appearance of Co precipitates. The EXAFS appeared to remain fcc-like. It should be pointed out that since the atomic numbers and hence electronic scattering effects of Co and Cu atoms are very similar, the analysis of the EXAFS in the studies referred to above was carried out as if there was only one type of scattering atom around the absorbing Co atom.

The existence of nanoscale fcc Co clusters in a variety of other metallic environments such as Ag and Nb has been widely reported by the Lyon group [68, 69, 89–92]. In the simplest case of a thick (1000 Å) film deposited purely from Co clusters [69], EXAFS in combination with x-ray diffraction and high resolution TEM indicated that the morphology consisted of a random stacking of fcc grains with diameters of 3–4 nm. The magnetic behaviour was consistent with a nanocrystalline structure and interpreted in terms of a random anisotropy model. In a Ag matrix, the Co clusters are also reported to adopt an fcc structure [89], with EXAFS measurements [93] indicating two local environments: atoms in the cluster core with the bulk separation, and surface atoms with an enlarged nearest neighbour distance. More recently, nanostructured films have been deposited from mixed Co–Ag clusters [91, 92]. From thermodynamic considerations, Ag is expected to segregate at the cluster surface; Ag and Co are immiscible, with Ag having a lower surface energy than Co, but a larger atomic radius. Consequently, a core–shell structure is expected with a Ag shell surrounding a magnetic Co core. Electron diffraction indicated that segregation does indeed occur, with both Ag and Co structures individually present,

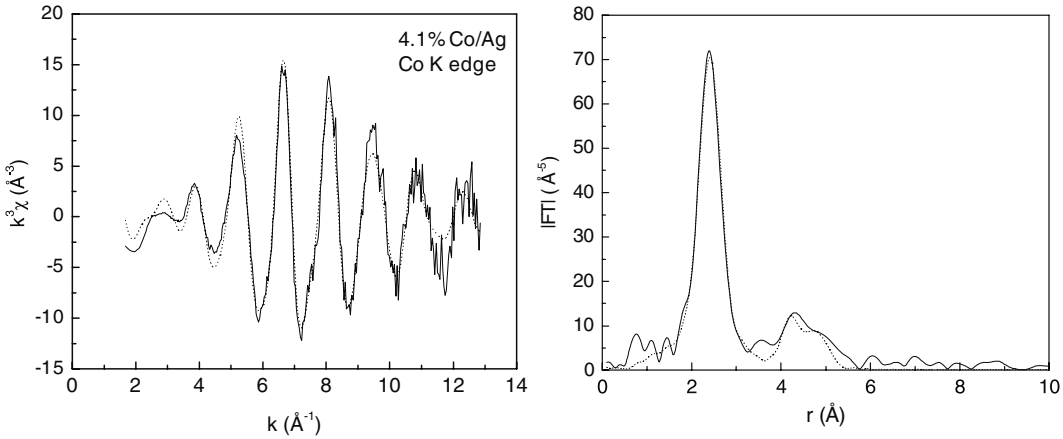

Figure 7. Co K edge EXAFS $k^3\chi$ and associated Fourier transform for a film consisting of 4.1% volume filling fraction (VFF) of Co clusters embedded in Ag.

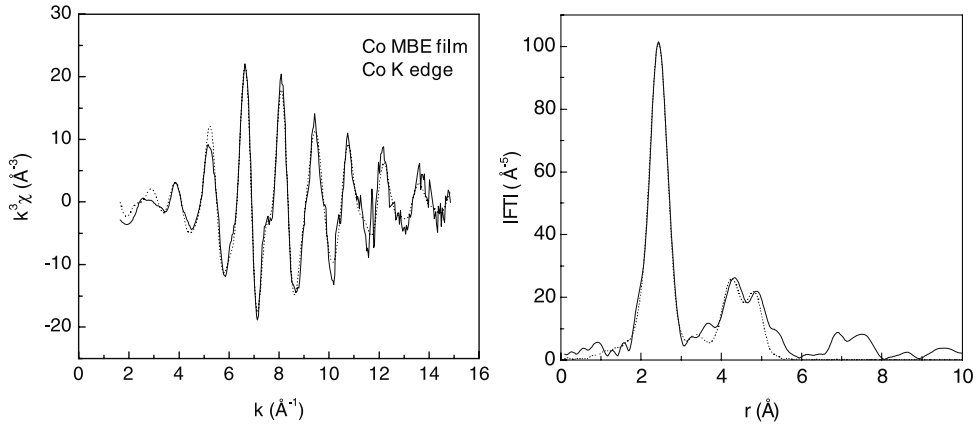

Figure 8. EXAFS $k^3\chi$ and associated Fourier transform for a Co MBE film.

Co apparently as fcc [91]. However, EXAFS measurements on Co–Ag clusters embedded in a dense MgO matrix revealed a strong Co–O contribution [91]. It therefore appears that segregation between the elements in the Co–Ag clusters is not perfect. This was reinforced by SQUID-magnetometry measurements which showed that the magnetization of Co–Ag clusters, clearly present when embedded in Nb, disappeared when embedded in MgO [91]; this could only be explained by the presence of Co–O bonds in the Co–Ag clusters. The above authors have also found strong evidence for a core–shell structure in Co clusters embedded in a Nb matrix [68, 90]. EXAFS measurements indicated that 70% of the Co atoms were surrounded by Co nearest neighbours at a bulk-like distance of ∼2.50 Å (taken to be in the fcc phase), while the remainder were surrounded by Nb neighbours at a distance of 2.58 Å (as in Co_6Nb_7) apart from 4% which had O nearest neighbours due to the presence of slight oxidation in the samples. These findings are consistent with a pure Co core in the clusters surrounded by an outer shell of CoNb alloy. Magnetization measurements provided further evidence for this [68]; a classical Langevin function was used to fit experimental magnetization curves for the Co cluster/Nb films in the superparamagnetic regime, which allowed the mean cluster diameter and dispersion to be deduced for the 'magnetic size' distribution. The size distribution measured magnetically was found to be lower than that measured directly from TEM images, which indicates that the CoNb alloy shell surrounding the Co core is 'magnetically dead'.

The existence of the fcc structure in embedded Co clusters, at least in a Ag matrix, is not completely supported by data elsewhere. Figure 7 shows EXAFS data measured by the present authors for a film containing 4.1% volume filling fraction (VFF) Co clusters in a Ag matrix [94]. Qualitatively, this looks similar to the data for the Co cluster film shown in figure 6, and also to data for a Co MBE film given in figure 8. The fit results for both films are consistent with hcp, as for the Co cluster film, and are given in table 1. In fact for the Co cluster/Ag film, fitting the data to either the hcp or fcc structure yields a nearest neighbour separation of 2.49 ± 0.01 Å (consistent with that for bulk Co). Fitting to hcp gives a better fit than to fcc, although the improvement is fairly small and possibly not statistically significant. This illustrates, at least, the difficulties that can be encountered in distinguishing between the hcp and fcc structures in EXAFS.

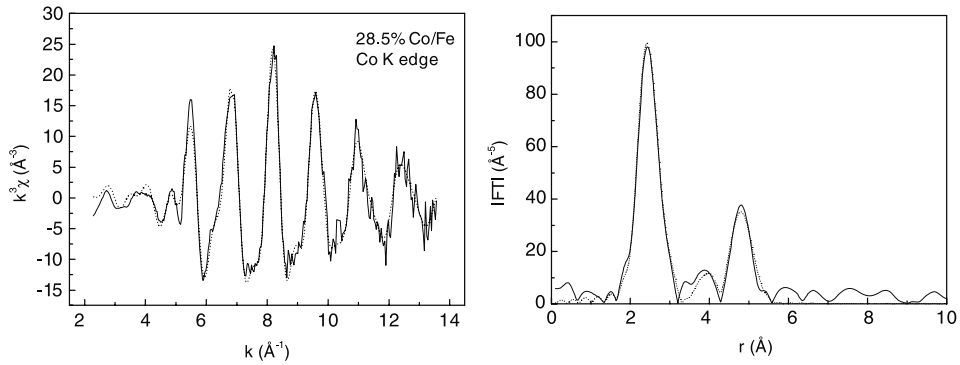

Figure 9. Co K edge EXAFS $k^3\chi$ and associated Fourier transform for a film comprising 28.5% VFF of Co clusters embedded in Fe. Reproduced with permission from [32]. Copyright 2006 IOP Publishing Ltd.

A matrix material in which the crystal structure of Co clusters clearly does switch to cubic from hcp is Fe, although the switch is to bcc rather than fcc. We have recently used EXAFS to show that Co clusters embedded in Fe adopt a bcc structure for cluster concentrations ranging from dilute values up to nearly 40% VFF [32]. Figure 9 shows the Co K edge EXAFS (weighted by k^3) and associated Fourier transform for a film containing 28.5% VFF of (bcc) Co clusters in Fe. Data analysis yielded a fit consistent with bcc. The fit parameters obtained are listed in table 2, along with the interatomic distances in bulk bcc Fe for comparison. (The coordinations were held fixed at bcc values during the fit, with the interatomic distances and Debye–Waller factors freely variable.) From the nearest neighbour distance we obtain a lattice parameter a of 2.83 ± 0.02 Å for the bcc Co clusters; this was found to be constant across the composition range investigated. This contrasts with the situation for the Co_xFe_{1-x} alloy system which has a bcc structure for $0 \leqslant x < 0.75$ [95] and for which, in this composition range, a decreases with increasing x from 2.87 Å for pure Fe to ∼2.83 Å for the most Co-rich bcc alloy. Hence, although it is not possible to rule out some alloying between Fe and Co at the cluster surfaces, the lack of variation in a across the studied composition range is consistent with a nanostructure of bcc Co clusters embedded in (bcc) Fe. Total energy calculations [80, 83] show that in Co bcc is a higher energy phase than hcp or fcc. Moreover, they also predict that the magnetic moments in bcc Co should be higher than in the other two phases.

5.2. *Fe clusters*

As discussed above for Co, there is also the potential in Fe to drive the atomic structure from the bcc phase adopted by the bulk at room temperature to a higher energy phase, and hence the possibility to 'engineer in' different magnetic properties. In particular, there has been much interest in fcc Fe. It is well known from many theoretical calculations [80, 96–102] that for bulk fcc Fe the magnetization undergoes a transition from a high to low spin state as the lattice parameter a is reduced, the transition occurring fairly sharply in the range $3.4\ \text{Å} \leqslant a \leqslant 3.7\ \text{Å}$. Bagayoko and Callaway [98], who considered only ferromagnetic solutions, find that the moment falls steadily to ∼2.6 μ_B as the lattice parameter decreases to $a \approx 3.6$ Å; in fact, the moments of both bcc and fcc structures are similar until that point. However below $a = 3.6$ Å the fcc moment falls rapidly to zero, with a decrease from 2.6 to 0.8 μ_B over a change in a of 0.2 Å, while the moment of the bcc structure decays much more slowly with decreasing a. Other authors find that a transition to an antiferromagnetic phase occurs at roughly the point that Bagayoko and Callaway [98] observed the onset of the rapid decrease in moment in their purely ferromagnetic calculation. Zhou *et al* [101, 102] predict as many as five different phases at different lattice parameters: a high spin ferromagnetic phase, two low spin ferromagnetic phases, an antiferromagnetic phase and a ferrimagnetic phase. However it is clear that the phases of lowest energy are successively ferromagnetic, antiferromagnetic and non-magnetic [80, 100, 103].

Although fcc Fe can only be stabilized above 1200 K in bulk form, it is now well established experimentally that ultra-thin fcc and fct Fe films can be grown epitaxially at lower temperatures on Cu [9–14], which has a lattice constant of 3.61 Å. A variety of techniques, including EXAFS [9], has been used to probe the atomic structure in these films. Both high moments (>2 μ_B/atom) and low moments (∼0.5 μ_B/atom) have been reported for fcc/fct films on the (100) [11, 12] and (111) [13, 14] surfaces of Cu.

The numerous reports dealing with fcc Fe films grown on Cu suggest that Cu should be a good matrix in which to embed fcc Fe clusters. EXAFS experiments performed on films of nanoscale Fe clusters in Cu [104, 105] show that this is indeed so. We have recently measured the atomic structure and net magnetic moments in ∼2 nm Fe clusters embedded in Cu as a function of cluster filling fraction using EXAFS and magnetometry respectively [105]. Figures 10 and 11 show Fe K edge EXAFS data for films containing 6.2% VFF and 26.6% VFF Fe clusters respectively. For the purposes of comparison, data for a bcc MBE Fe film is also shown in figure 12. A fit consistent with fcc was obtained for the 6.2% VFF film, while for the 26.6% VFF film (and Fe MBE film) bcc fits were obtained. The fit parameters obtained are given in table 2 along with the interatomic distances in bulk fcc Fe. For the 6.2% VFF film, and in fact for cluster filling fractions less than ∼25% VFF, we find that the embedded Fe clusters have an fcc structure with $a = 3.58 \pm 0.02$ Å (obtained from the

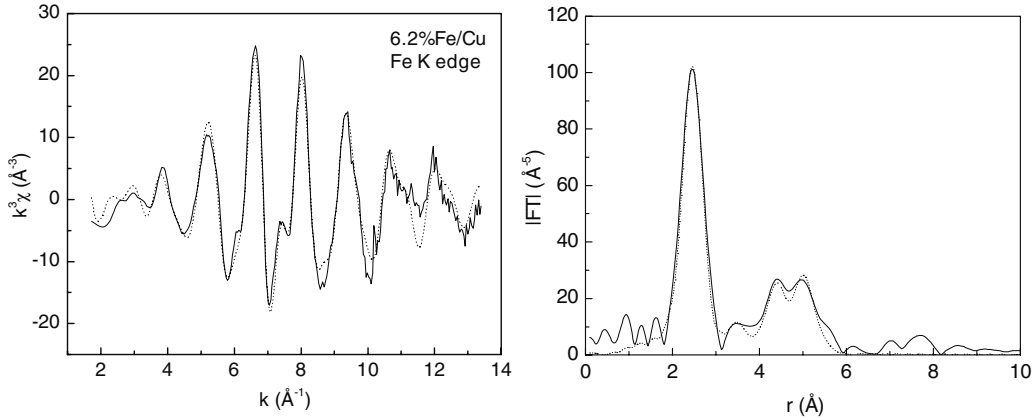

Figure 10. Fe K edge EXAFS $k^3\chi$ and associated Fourier transform for a film comprising 6.2% VFF of Fe clusters embedded in Cu. Reproduced with permission from [105]. Copyright 2008 by the American Physical Society.

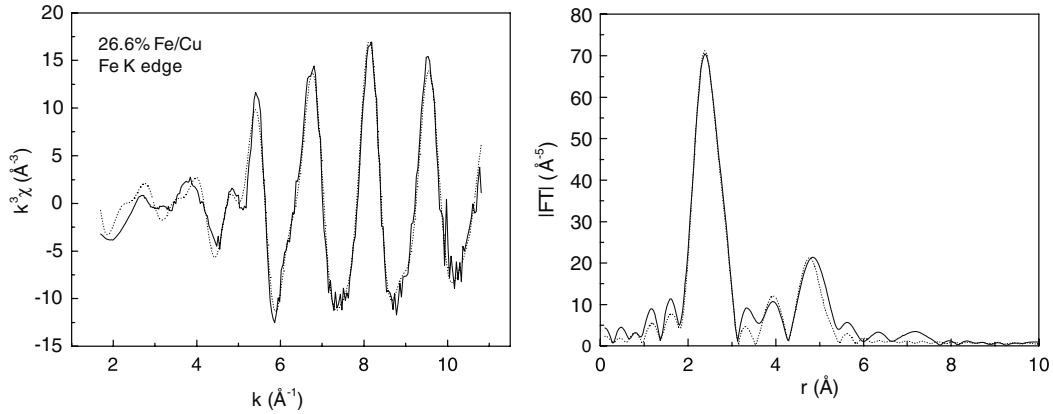

Figure 11. Fe K edge EXAFS $k^3\chi$ and associated Fourier transform for a film comprising 26.6% VFF of Fe clusters embedded in Cu. Reproduced with permission from [105]. Copyright 2008 by the American Physical Society.

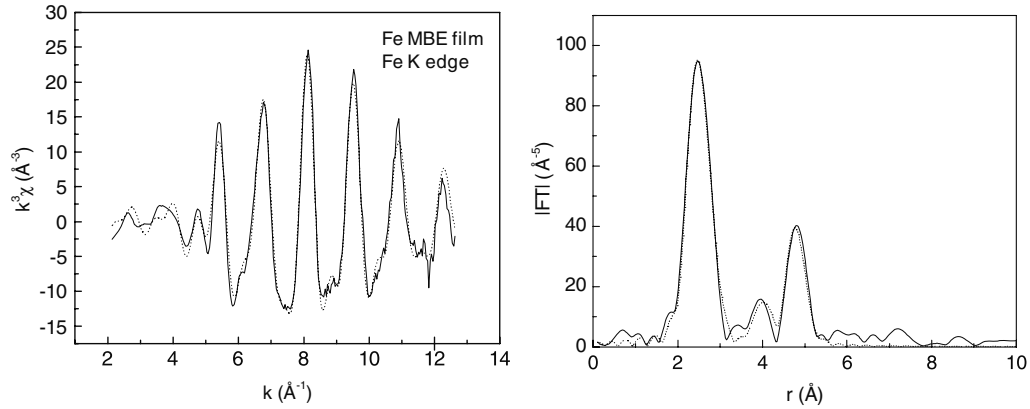

Figure 12. EXAFS $k^3\chi$ and associated Fourier transform for an Fe MBE film.

nearest neighbour distance) while above this they adopt the bulk Fe bcc structure. We note that the three-dimensional percolation threshold is 24.88% [106]; it therefore appears that as larger (interconnected) agglomerates of Fe clusters occur in the nanocomposite film as the cluster fraction approaches this value, the fcc structure can no longer be maintained. The net magnetic moment in the Fe clusters switches sharply as their crystal structure changes across the percolation threshold, from the bulk Fe value of 2.2±0.02 to 0.4–0.9 μ_B/atom, as indicated in figure 13.

Table 2. Structural parameters r_j, $2\sigma_j^2$ (interatomic distance, Debye–Waller factor respectively) obtained from fits to the Co K edge EXAFS for a 28.5% VFF Co/Fe film, and Fe K edge EXAFS for a 6.2% VFF Fe/Cu film, a 26.6% VFF Fe/Cu film and an Fe MBE film. Also included are the interatomic distances and coordinations N_j for bcc and fcc bulk Fe. The coordinations were held fixed at bcc, or fcc, values during the fits.

	Shell 1	Shell 2	Shell 3	Shell 4	Shell 5
28.5% VFF Co/Fe	$r_1 = 2.45 \pm 0.01$ Å	$r_2 = 2.84 \pm 0.02$ Å	$r_3 = 4.05 \pm 0.02$ Å	$r_4 = 4.73 \pm 0.02$ Å	$r_5 = 4.94 \pm 0.02$ Å
(Co K edge)	$2\sigma_1^2 = 0.011 \pm 0.001$ Å^2	$2\sigma_2^2 = 0.023 \pm 0.003$ Å^2	$2\sigma_3^2 = 0.027 \pm 0.004$ Å^2	$2\sigma_4^2 = 0.024 \pm 0.004$ Å^2	$2\sigma_5^2 = 0.021 \pm 0.003$ Å^2
Bulk bcc Fe	$r_1 = 2.49$ Å	$r_2 = 2.87$ Å	$r_3 = 4.06$ Å	$r_4 = 4.76$ Å	$r_5 = 4.97$ Å
	$N_1 = 8$	$N_2 = 6$	$N_3 = 12$	$N_4 = 24$	$N_5 = 8$
MBE Fe film	$r_1 = 2.49 \pm 0.01$ Å	$r_2 = 2.86 \pm 0.02$ Å	$r_3 = 4.12 \pm 0.02$ Å	$r_4 = 4.80 \pm 0.01$ Å	
	$2\sigma_1^2 = 0.011 \pm 0.001$ Å^2	$2\sigma_2^2 = 0.020 \pm 0.003$ Å^2	$2\sigma_3^2 = 0.023 \pm 0.004$ Å^2	$2\sigma_4^2 = 0.014 \pm 0.002$ Å^2	
26.6% VFF Fe/Cu	$r_1 = 2.49 \pm 0.01$ Å	$r_2 = 2.84 \pm 0.03$ Å	$r_3 = 4.11 \pm 0.03$ Å	$r_4 = 4.78 \pm 0.02$ Å	
	$2\sigma_1^2 = 0.012 \pm 0.001$ Å^2	$2\sigma_2^2 = 0.036 \pm 0.008$ Å^2	$2\sigma_3^2 = 0.031 \pm 0.008$ Å^2	$2\sigma_4^2 = 0.022 \pm 0.004$ Å^2	
6.2% VFF Fe/Cu	$r_1 = 2.53 \pm 0.01$ Å	$r_2 = 3.55 \pm 0.03$ Å	$r_3 = 4.43 \pm 0.02$ Å	$r_4 = 5.08 \pm 0.02$ Å	
	$2\sigma_1^2 = 0.015 \pm 0.001$ Å^2	$2\sigma_2^2 = 0.026 \pm 0.008$ Å^2	$2\sigma_3^2 = 0.027 \pm 0.004$ Å^2	$2\sigma_4^2 = 0.021 \pm 0.003$ Å^2	
Bulk fcc Fe	$r_1 = 2.54$ Å	$r_2 = 3.59$ Å	$r_3 = 4.40$ Å	$r_4 = 5.08$ Å	$r_5 = 5.68$ Å
	$N_1 = 12$	$N_2 = 6$	$N_3 = 24$	$N_4 = 12$	$N_5 = 24$

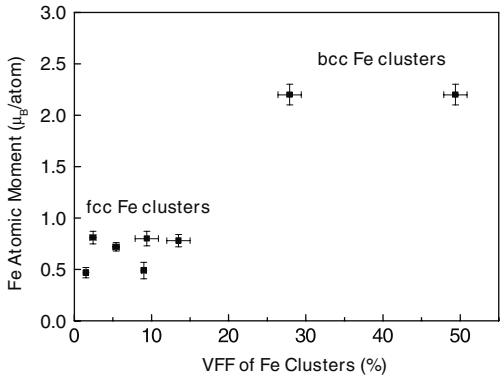

Figure 13. Net atomic moment in Fe clusters embedded in Cu as a function of volume filling fraction (VFF) of Fe clusters. Reproduced with permission from [105]. Copyright 2008 by the American Physical Society.

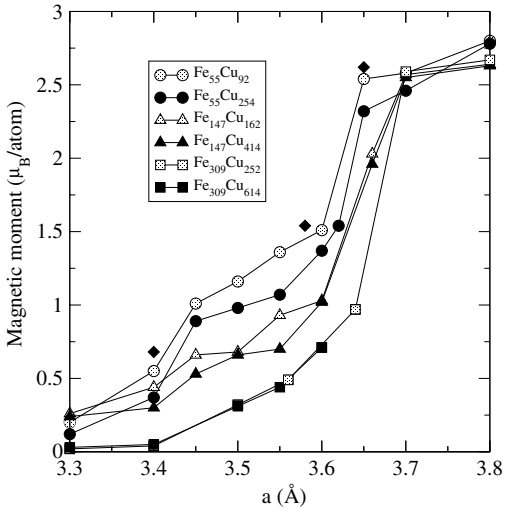

Figure 14. Calculated spin moment of fcc Fe clusters (55, 147, and 309 atoms), embedded in one and two shells of Cu, as a function of a (the size of the cubic unit cell). Data points joined by lines are from tight-binding calculations. *Ab initio* results for the $Fe_{55}Cu_{92}$ cluster are indicated by the filled diamonds. Reproduced with permission from [105]. Copyright 2008 by the American Physical Society.

The values measured by us for the net magnetic moments in the nanocomposite Fe/Cu films are in excellent agreement with those predicted from spin-polarized electronic structure calculations on Cu-embedded fcc Fe clusters, also performed by us [105]. Using *ab initio* and tight-binding techniques, the calculations were performed on Fe particle/Cu shell clusters and investigated the magnetism as a function of lattice constant and Cu shell thickness. (Fe core/Cu shell clusters were studied since it is not realistic to perform calculations on particles of the size studied experimentally.) Without any experimental information about the cluster shapes, we therefore confined the calculations to fcc cuboctahedral clusters with O_h symmetry of the form Fe_mCu_{m-n}, where m and n are 'magic numbers' for the cuboctahedral system: 55, 147, 309, 561, 923, and $n > m$. Our main interest is at $m = 147$ and 309 since these numbers straddle the size in our EXAFS and magnetometry experiments. Further details relating to the computational methods may be found in [105]. Figure 14 shows the calculated spin moment of the Fe clusters embedded in one and two shells of Cu; the results are displayed as a function of lattice parameter. At large lattice parameters we obtain high moments, a little over 2.5 μ_B; this is very close to values that we have also calculated for the corresponding bare Fe clusters. As the lattice parameter decreases, the moment decreases sharply; in the low moment regime at smaller lattice spacings, the net moments are less than in the corresponding bare Fe clusters. Comparing the various plots in figure 14, we note that the moment per atom decreases as the cluster size increases. Also, it appears that a second Cu shell has a decreasing influence on the Fe moment as the cluster size increases.

As described above, from EXAFS measurements we have determined a lattice parameter of 3.58 ± 0.02 Å for fcc Fe clusters embedded in Cu. From figure 14, the values of magnetic moments for the 147 and 309 atom clusters (which straddle the experimental size) at $a = 3.58$ Å can be read off from the plots to provide an estimate of 0.4–0.8 μ_B for the net atomic moment. This agrees rather well with the measured value of 0.4–0.9 μ_B/atom. As far as individual atomic moments are concerned, the calculations provide a picture of up and down spin local moments. We find that the moments on Fe atoms that interface with the Cu coating generally align parallel with each other, but that there is a greater cancellation between up and down spins in the Fe core. However, the net atomic moment (plotted in figure 14) is consistent with experimental observation (at least for $a = 3.58$ Å). The alignment of individual atomic moments is discussed at greater length in [105].

The calculations referred to above [105] indicate that if a can be increased from the measured value of 3.58 Å towards 3.7 Å, the atomic moments in the embedded fcc Fe nanoclusters should approach the high spin value (∼2.5 μ_B). Embedding Fe clusters in an fcc metal with a larger value of a than Cu might be a means of achieving this. For this reason, we have recently used EXAFS to examine the structure of Fe clusters embedded in Pd [107], for which $a = 3.89$ Å. Figure 15 shows Fe K edge EXAFS data for a sample containing 3.8% VFF Fe clusters in Pd. The data is consistent with alloying at the interface between the clusters and the matrix. Details of the analysis of the EXAFS for the Fe cluster/Pd system will be published elsewhere [107]. In short, however, the clusters effectively have a core–shell structure, with an FePd alloy shell surrounding a pure Fe core. A three-shell fit to the spectrum for the 3.8% VFF Fe sample in figure 15 yields nearest neighbour distances in the alloy shell of 2.69 ± 0.01 Å and 2.71 ± 0.02 Å for r_{Fe-Pd} and r_{Fe-Fe} respectively, consistent with the nearest neighbour distance of 2.69 Å in the disordered fcc $Fe_{0.5}Pd_{0.5}$ alloy and also in close agreement with values measured in MBE-grown films of FePd alloys [107]. In the Fe core, a nearest neighbour separation r_{Fe-Fe} of 2.53 ± 0.02 Å is obtained for this sample which would imply an fcc lattice parameter of 3.58 ± 0.03 Å i.e. no larger than the value measured for Cu-embedded fcc Fe clusters [105]. With increasing cluster concentration, r_{Fe-Fe} in the Fe core drops to values intermediate between that for bcc

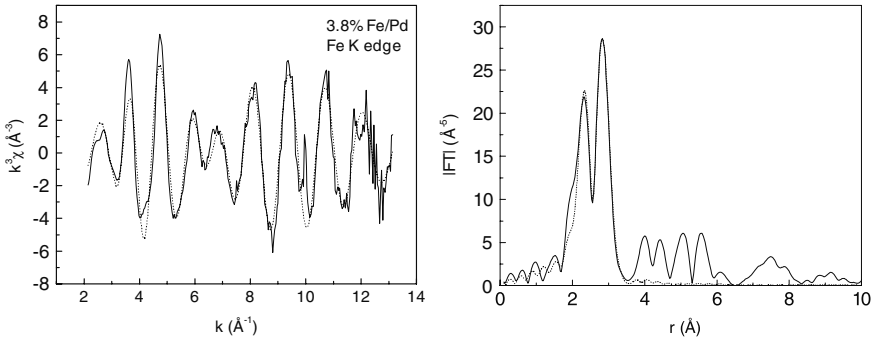

Figure 15. Fe K edge EXAFS $k^3\chi$ and associated Fourier transform for a film comprising 3.8% VFF of Fe clusters embedded in Pd.

bulk Fe and (non-alloyed) fcc Fe clusters in Cu [105], making it difficult to determine which structure the Fe cores adopt; for cluster filling fractions greater than ∼20% VFF, however, the nearest neighbour distance is close to the bcc value.

Alloying at the interface between the Fe clusters and the matrix complicates the EXAFS analysis, as in the case of a Pd matrix described above. There is also the possibility that the alloyed outer shell is non-magnetic, as described earlier for Co clusters in Nb [68, 90]. Attempts to stabilize the fcc structure in Fe clusters by embedding them in a non-alloying fcc metal with an appreciably larger lattice parameter than Pd have not been successful. In Ag for example, for which $a = 4.09$ Å, several authors [48, 104] have demonstrated using EXAFS that Fe clusters have a bcc structure with the same value of a as in bulk Fe. This is in fact not too surprising since the lattice parameters of Ag and bcc Fe ($a = 2.87$ Å) differ almost exactly by a factor $\sqrt{2}$; hence, after a rotation of 45° about the surface normal, there is nearly perfect registry between the Fe(100) and Ag(100) surfaces. A promising matrix material in which to stabilize fcc Fe clusters, which should avoid problems associated with alloying at the cluster surface, is the $Cu_{1-x}Au_x$ alloy system. This has the added advantage that by varying the composition in the range $0 \leqslant x \leqslant 0.2$, the lattice parameter can be varied between 3.61 Å (for pure Cu) to ∼3.70 Å (for $x = 0.2$) while maintaining an fcc structure. Indeed, a number of authors [108–110] have used $Cu_{1-x}Au_x(100)$ alloy substrates to grow ultra-thin fcc Fe films with expanded lattice parameter. Embedding Fe clusters in a $Cu_{1-x}Au_x$ matrix should therefore allow fine tuning of the fcc Fe lattice parameter. EXAFS and magnetometry measurements could then be used to establish the maximum lattice parameter and maximum magnetic moment that could be realized in fcc Fe clusters.

6. Conclusions

This paper has tried to show that the element-specific and non-invasive nature of EXAFS make it an ideal probe of atomic structure in nanostructured materials, particularly for magnetic cluster-assembled films comprised of magnetic nanosized clusters embedded in a metal matrix. Combining and correlating structural data with magnetic measurements is a good means to obtain an insight into new magnetic materials, especially when coupled with theoretical calculations specific to the nanostructure under study. It is increasingly likely that novel core–shell clusters, deposited directly from a cluster source rather than forming as a result of alloying at the cluster/matrix interface, will form the building blocks for new magnetic cluster-assembled materials. The strengths of the EXAFS technique in probing atomic structure in this new class of nanoclusters are evident.

Acknowledgments

Work by the Leicester group presented in this review was supported by EC grants ANMARE (contract number G5RD-CT-2001-00478) and NANOSPIN (contract number NMP4-CT-2004-013545). The authors are grateful to S Fiddy at Daresbury Laboratory for his assistance during EXAFS experiments.

References

[1] Perez A, Melinon P, Dupuis V, Jensen P, Prevel B, Tuaillon J, Bardotti L, Martet C, Treilleux M, Broyer M, Pellarin M, Vialle J L, Palpant B and Lerme J 1997 *J. Phys. D: Appl. Phys.* **30** 709
[2] Methling R-P, Senz V, Klingenberg E-D, Diederich Th, Tiggesbäumker J, Holzhütter G, Bannsman J and Meiwes-Broer K H 2001 *Eur. Phys. J.* D **16** 173
[3] Binns C, Trohidou K N, Bansman J, Baker S H, Blackman J A, Bucher J P, Kechrakos D, Kleibert A, Louch S, Meiwes-Broer K H, Pastor G M, Perez A and Xie Y 2005 *J. Phys. D: Appl. Phys.* **38** R357
[4] Billas I M L, Becker J A, Châtelain A and de Heer W A 1993 *Phys. Rev. Lett.* **71** 4067
[5] Edmonds K W, Binns C, Baker S H, Maher M J, Thornton S C, Tjernberg O and Brookes N B 2001 *J. Magn. Magn. Mater.* **231** 113
[6] Baker S H, Binns C, Edmonds K W, Maher M J, Thornton S C, Louch S and Dhesi S S 2002 *J. Magn. Magn. Mater.* **247** 19
[7] Lau J T, Fohlisch A, Nietubye R, Rief M and Wurth W 2002 *Phys. Rev. Lett.* **89** 057201
[8] Edmonds K W, Binns C, Baker S H, Maher M J, Thornton S C, Tjernberg O and Brookes N B 2000 *J. Magn. Magn. Mater.* **220** 25
[9] Magnan H, Chandesris D, Villette B, Heckmann O and Lecante J 1991 *Phys. Rev. Lett.* **67** 859
[10] Müller S, Bayer P, Reischl C, Heinz K, Feldmann B, Zillgen H and Wuttig M 1995 *Phys. Rev. Lett.* **74** 765
[11] Ellerbrock R D, Fuest A, Schatz A, Keune W and Brand R A 1995 *Phys. Rev. Lett.* **74** 3053

[12] Schmitz D, Charton C, Scholl A, Carbone C and Eberhardt W 1999 *Phys. Rev.* B **59** 4327
[13] Shen J, Klaua M, Ohresser P, Jenniches H, Barthel J, Mohan Ch V and Kirschner J 1997 *Phys. Rev.* B **56** 11134
[14] Shen J, Ohresser P, Mohan Ch V, Klaua M, Barthel J and Kirschner J 1998 *Phys. Rev. Lett.* **80** 1980
[15] Gurman S J 1982 *J. Mater. Sci.* **17** 1541
[16] Hayes T M and Boyce J B 1983 *Solid State Phys.* **37** 173
[17] Koningsberger D C and Prins R 1988 *X-ray Absorption* (Chichester: Wiley)
[18] Gurman S J 1990 in *Synchrotron Radiation and Biophysics* ed S S Hasnain (Chichester: Ellis Horwood) pp 9–42
[19] Gurman S J 1995 *J. Synchrotron Radiat.* **2** 56
[20] Wang J-Q, Xiong P and Xiao G 1993 *Phys. Rev.* B **47** 8341
[21] Berkowitz A E, Mitchell J R, Carey M J, Young A P, Zhang S, Spada F E, Parker F T, Hutten A and Thomas G 1992 *Phys. Rev. Lett.* **68** 3745
[22] Meng W J, Zhang X D, Shi B, Jiang J C, Rehn L E, Baldo P M and Tittsworth R C 2003 *Surf. Coat. Technol.* **163/164** 251
[23] García Prieto A, Fdez-Gubieda M L, García-Arribas A, Barandiarán J M, Meneghini C and Mobilio S 2000 *J. Magn. Magn. Mater.* **221** 80
[24] Vergara M P C, Cezar J C, Tolentino H C N and Knobel M 2002 *Physica* B **320** 143
[25] Sheng H W, Hu Z Q and Lu K 1997 *Nanostruct. Mater.* **9** 661
[26] Davis R J and Boudart M 1994 *J. Phys. Chem.* **98** 5471
[27] Reifsnyder S N and Lamb H H 1999 *J. Phys. Chem.* **103** 321
[28] Prins R and Cimini F 1997 *J. Phys. Chem.* **101** 5285
[29] Binns C 2001 *Surf. Sci. Rep.* **44** 1
[30] de Heer W A 1993 *Rev. Mod. Phys.* **65** 611
[31] Milani P and Iannotta S 1999 *Cluster Beam Synthesis of Nanostructured Materials* (Berlin: Springer)
[32] Baker S H, Roy M, Louch S and Binns C 2006 *J. Phys.: Condens. Matter* **18** 2385
[33] Rubin S, Holdenried M and Micklitz H 1998 *Eur. Phys. J.* B **5** 23
[34] Baker S H, Thornton S C, Edmonds K W, Maher M J, Norris C and Binns C 2000 *Rev. Sci. Instrum.* **71** 3178
[35] Elliott S R 1990 *Physics of Amorphous Materials* 2nd edn (Harlow: Longman)
[36] Baker S H, Roy M, Louch S and Binns C 2005 unpublished data
[37] Stern E A 1974 *Phys. Rev.* B **10** 3027
[38] Lee P A and Pendry J B 1975 *Phys. Rev.* B **11** 2795
[39] Gurman S J, Binsted N and Ross I 1984 *J. Phys. C: Solid State Phys.* **17** 143
[40] Sarode P R, Priolkar K R, Bera P, Hegd M S, Emura S and Kumashiro R 2002 *Mater. Res. Bull.* **37** 1679
[41] Binsted N 1998 *EXCURV98: Daresbury Laboratory Computer Program*
[42] Stern E A, Newville M, Ravel B, Yacoby Y and Haskel D 1995 *Physica* B **208/209** 117
[43] Newville M 2001 *J. Synchrotron Radiat.* **8** 322
[44] Roy M and Gurman S J 2001 *J. Synchrotron Radiat.* **8** 1095
[45] Cluskey P D, Newport R J, Benfield R E, Gurman S J and Schmid G 1993 *Z. Phys.* D **26** S8–S11
[46] Benfield R E, Grandjean D, Kröll M, Pugin R, Sawitowski T and Schmid G 2001 *J. Phys. Chem.* B **105** 1961
[47] Frenkel A I, Hills C W and Nuzzo R G 2001 *J. Phys. Chem.* B **105** 12689
[48] Baker S H, Roy M, Gurman S J, Louch S, Bleloch A and Binns C 2004 *J. Phys.: Condens. Matter* **16** 7813
[49] Tranquada J M and Ingalls R 1983 *Phys. Rev.* B **28** 3520
[50] Sandstrom D R, Marques E C, Biebesheimer V A, Lytle F W and Greegor R B 1985 *Phys. Rev.* B **32** 3541
[51] Pinto A, Pennisi A R, Faraci G, D'Agostino G, Mobilio S and Boscherini F 1995 *Phys. Rev.* B **51** 5315
[52] Stern E A and Heald S M 1983 *Handbook on Synchrotron Radiation* vol 1, ed E E Koch (New York: North-Holland)
[53] Fairbanks M C, Benfield R E, Newport R J and Schmid G 1990 *Solid State Commun.* **73** 431
[54] Akolekar Deepak B, Bhargava Suresh K, Foran Garry and Takahashi Masashi 2005 *J. Mol. Catal.* A **238** 78
[55] Balerna A, Bernieri E, Picozzi P, Reale A, Santucci S, Burattini E and Mobilio S 1985 *Phys. Rev.* B **31** 5058
[56] Reifsnyder S N, Otten M M, Sayers D E and Lamb H H 1997 *J. Phys. Chem.* B **101** 4972
[57] Sarode P R, Priolkar K R, Bera P, Hegde M S, Emura S and Kumashiro R 2002 *Mater. Res. Bull.* **37** 1679
[58] Gota S, Gautier M, Douillard L, Thromat N, Duraud J P and Le Fèvre P 1995 *Surf. Sci.* **323** 163
[59] Sinfelt J H 1972 *Chem. Eng. News* **50** 18
[60] Sinfelt J H 1973 *J. Catal.* **29** 308
[61] Lam Y L, Criado J and Boudart M 1977 *Nouv. J. Chim.* **1** 461
[62] Biloen P, Helle J N, Verbeek H, Dautzenberg F M and Sachtler W M H 1980 *J. Catal.* **63** 112
[63] Burch R and Garla L C 1981 *J. Catal.* **71** 360
[64] Shum V K, Butt J B and Sachtler W M H 1986 *J. Catal.* **99** 126
[65] Davis Robert J and Boudart Michel 1994 *J. Phys. Chem.* **98** 5471
[66] Reifsnyder S N and Lamb H H 1999 *J. Phys. Chem.* **103** 321
[67] Cimini F and Prins R 1997 *J. Phys. Chem.* **101** 5285
[68] Jamet M, Dupuis V, Mélinon P, Guiraud G, Pérez A, Wernsdorfer W, Traverse A and Baguenard B 2000 *Phys. Rev.* B **62** 493
[69] Tuaillon J, Dupuis V, Mélinon P, Prével B, Treilleux M, Perez A, Pellarin M, Vialle J L and Broyer M 1997 *Phil. Mag.* A **76** 493
[70] Stern E A, Siegel R W, Newville M, Sanders P G and Haskel D 1995 *Phys. Rev. Lett.* **75** 3874
[71] Haubold T, Birringer R, Lengeler B and Gleiter H 1989 *Phys. Lett.* A **135** 461
[72] di Cicco A, Berrettoni M, Stizza S, Bonetti E and Cocco G 1994 *Phys. Rev.* B **50** 12386
[73] de Panfilis S, d'Acapito F, Haas V, Konrad H, Weissmüller J and Boscherini F 1995 *Phys. Lett.* A **207** 397
[74] Siegel R W and Fougere G E 1995 *Nanostruct. Mater.* **6** 205
[75] Kuboyashi S, Takahasi T and Sasaki J 1972 *J. Phys. Soc. Japan* **32** 1234
[76] Kubo R 1962 *J. Phys. Soc. Japan* **17** 975
[77] Douglass D C, Cox A J, Bucher J P and Bloomfield L A 1993 *Phys. Rev.* B **47** 12874
[78] Marcus P M and Moruzzi V L 1985 *Solid State Commun.* **55** 971
[79] Moruzzi V L, Marcus P M, Schwarz K and Mohn P 1986 *J. Magn. Magn. Mater.* **54–57** 955
[80] Moruzzi V L, Marcus P M, Schwarz K and Mohn P 1986 *Phys. Rev.* B **34** 1784
[81] Paxton A T, Methfessel M and Polatoglou H M 1990 *Phys. Rev.* B **41** 8127
[82] Trgg J, Johansson B, Eriksson O and Wills J M 1995 *Phys. Rev. Lett.* **75** 2871
[83] Guo G Y and Wang H H 2000 *Chin. J. Phys.* **38** 949
[84] Harp G R, Farrow R F C, Weller D, Rabedeau T A and Marks R F 1993 *Phys. Rev.* B **48** 17538
[85] Berkowitz A E, Mitchell J R, Carey M J, Young A P, Zhang S, Spada F E, Parker F T, Hutten A and Thomas G 1992 *Phys. Rev. Lett.* **68** 3745
[86] Xiao J Q, Jiang J S and Chien C L 1992 *Phys. Rev. Lett.* **68** 3749
[87] Cezar J C, Tolentino H C N and Knobel M 2001 *J. Magn. Magn. Mater.* **233** 103
[88] Cezar J C, Tolentino H C N and Knobel M 2003 *Phys. Rev.* B **68** 0544041

[89] Dupuis V, Tuaillon J, Prevel B, Perez A, Melinon P, Guiraud G, Parent F, Steren L B, Morel R, Barthelemy A, Fert A, Mangin S, Thomas L, Wernsdorfer W and Barbara B 1997 *J. Magn. Magn. Mater.* **165** 42
[90] Dupuis V, Jamet M, Favre L, Tuiallon-Combes J, Melinon P and Perez A 2003 *J. Vac. Sci. Technol.* A **21** 1519
[91] Favre L, Stanescu S, Dupuis V, Bernstein E, Epicier T, Melinon P and Perez A 2004 *Appl. Surf. Sci.* **226** 265
[92] Dupuis V, Favre L, Stanescu S, Tuiallon-Combes J, Bernstein E and Perez A 2004 *J. Phys.: Condens. Matter* **16** S2231
[93] Tuiallon J 1995 *PhD Thesis* University Lyon I France
[94] Baker S H, Roy M and Binns C 2006 unpublished data
[95] Ellis W C and Greiner E S 1941 *Am. Soc. Met.* **29** 415
[96] Andersen O K, Madsen U, Poulsen U K, Jepsen O and Kollar J 1977 *Physica* B **86–88** 249
[97] Kübler J 1981 *Phys. Lett.* A **81** 81
[98] Bagayoko D and Callaway J 1983 *Phys. Rev.* B **28** 5419
[99] Krasko G 1987 *Phys. Rev.* B **36** 8565
[100] Guenzburger D and Ellis D E 1995 *Phys. Rev.* B **51** 1519
[101] Zhou Y-M, Zhang W-Q, Zhong L-P and Weng D-S 1995 *J. Magn. Magn. Mater.* **145** L273
[102] Zhou Y-M, Zhang W-Q, Zhong L-P and Weng D-S 1997 *J. Magn. Magn. Mater.* **167** 136
[103] Moruzzi V L, Marcus P M and Kübler J 1989 *Phys. Rev.* B **39** 6957
[104] Sakurai M, Makhlouf S A, Hihara T, Sumiyama K, Wakoh K and Suzuki K 1995 *Physica* B **208/209** 614
[105] Baker S H, Asaduzzaman A M, Roy M, Gurman S J, Binns C, Blackman J A and Xie Y 2008 *Phys. Rev.* B **78** 014422
[106] Stauffer D and Aharony A 1994 *Introduction to Percolation Theory* (London: Taylor and Francis)
[107] Baker S H, Roy M and Binns C 2007 unpublished data
[108] Gradmann U and Isbert H O 1980 *J. Magn. Magn. Mater.* **15–18** 1109
[109] Mitani S, Kida A and Matsui M 1993 *J. Magn. Magn. Mater.* **126** 76
[110] Keavney D J, Storm D F, Freeland J W, Grigorov I L and Walker J C 1995 *Phys. Rev. Lett.* **74** 4531